

Adsorption and Solar Light Decomposition of Acetone on Anatase TiO₂ and Niobium Doped TiO₂ Thin Films

Andreas Mattsson,[†] Michael Leideborg,[‡] Karin Larsson,[‡] Gunnar Westin,[‡] and Lars Österlund^{*,†}

Department of Environment and Protection, FOI NBC Defence, SE-901 82 Umeå, Sweden, and Department of Materials Chemistry, Ångström Laboratory, Uppsala University, SE-751 21 Uppsala, Sweden

Received: October 4, 2005; In Final Form: November 3, 2005

Adsorption and solar light decomposition of acetone was studied on nanostructured anatase TiO₂ and Nb-doped TiO₂ films made by sol–gel methods (10 and 20 mol % NbO_{2.5}). A detailed characterization of the film materials show that films contain only nanoparticles with the anatase modification with pentavalent Nb oxide dissolved into the anatase structure, which is interpreted as formation of substituted Nb=O clusters in the anatase lattice. The Nb-doped films displayed a slight yellow color and an enhanced the visible light absorption with a red-shift of the optical absorption edge from 394 nm for the pure TiO₂ film to 411 nm for 20 mol % NbO_{2.5}. In-situ Fourier transform infrared (FTIR) transmission spectroscopy shows that acetone adsorbs associatively with η^1 -coordination to the surface cations on all films. On Nb-doped TiO₂ films, the carbonyl bonding to the surface is stabilized, which is evidenced by a lowering of the $\nu(\text{C}=\text{O})$ frequency by about 20 cm⁻¹ to 1672 cm⁻¹. Upon solar light illumination acetone is readily decomposed on TiO₂, and stable surface coordinated intermediates are formed. The decomposition rate is an order of magnitude smaller on the Nb-doped films despite an enhanced visible light absorption in these materials. The quantum yield is determined to be 0.053, 0.004 and 0.002 for the pure, 10% Nb:TiO₂, and 20%Nb:TiO₂, respectively. Using an interplay between FTIR and DFT calculations we show that the key surface intermediates are bidentate bridged formate and carbonate, and H-bonded bicarbonate, respectively, whose concentration on the surface can be correlated with their heats of formation and bond strength to coordinatively unsaturated surface Ti and Nb atoms at the surface. The oxidation rate of these intermediates is substantially slower than the initial acetone decomposition rate, and limits the total oxidation rate at $t > 7$ min on TiO₂, while no decrease of the rate is observed on the Nb-doped films. The rate of degradation of key surface intermediates is different on pure TiO₂ and Nb-doped TiO₂, but cannot explain the overall lower total oxidation rate for the Nb-doped films. Instead the inferior photocatalytic activity in Nb-doped TiO₂ is attributed to an enhanced electron–hole pair recombination rate due to Nb=O cluster and cation vacancy formation.

1. Introduction

Titanium dioxide photocatalysis has for the past three decades been a promising technology for air and water remediation.^{1–4} This field is now maturing into a viable commercial technology, where a broadened application area includes coating technology and maintenance-free surfaces in general. The wide band gap of TiO₂ (3.2 and 3.0 eV for anatase and rutile, respectively) necessitates, however, UV light to excite electrons over the band gap. In many applications, including those utilizing solar light as the energy source, it is desirable to exploit a larger portion of the spectrum, i.e., to extend the band gap excitations into the visible regime. A second generation of efficient UV–visible active photocatalytic materials are therefore currently sought where doped TiO₂ has received considerable attention.⁵ Several methods and materials have been employed, including anion doping by replacing lattice oxygen with N,^{6,7} C,^{8,9} F,^{10,11} or S,¹² and cation doping, whereby Ti cations are substituted with, e.g., V, Cr, Mn, Fe, and Ni atoms.⁵ Other candidates for visible active materials are binary oxides^{5,13} and perovskites.¹⁴ It is a delicate

matter to introduce dopants into TiO₂ to lower the optical band gap energy, while at the same time avoiding creation of unwanted recombination centers or localized band gap states, which prevent efficient separation of excited electron–hole pairs. Furthermore, a slight lowering of the conduction band may place the conduction band edge below the O₂ affinity level (O₂/O₂⁻), thus jeopardizing the formation of oxygen radicals, which are key intermediates in photocatalytic oxidation (PCO) reactions.³

In the present paper, we explore the potential of using Nb doped TiO₂ as a visible active photocatalytic material. Niobium oxide and, in particular, its most stable form, Nb₂O₅, is an interesting semiconductor with a band gap of about 3.9 eV (decreasing to about 3.5 eV in the amorphous state¹⁵), with a high dielectric constant and a high index of refraction, which has found important applications in electronics and optical applications, including thin films (antireflective coatings, solar control, etc.¹⁶). In a recent report,¹⁷ it was shown that Nb doped anatase yields films with high electron conductivity, which are interesting in, e.g., photoelectrochemical systems. In the present paper, we present results for sol–gel synthesized Nb doped anatase films, which we previously also have shown to have

* Corresponding author. Email: lars.osterlund@foi.se. Tel: +46 90 106900. Fax: +46 90 106802.

[†] FOI NBC Defence.

[‡] Uppsala University.

high conductivity, and explore their use as a potential photocatalyst material.

Thermal and photochemical reactions with acetone have been subjected to a large number of studies, because of its importance as a reactant, intermediate, and product in many fine chemical or catalytic oxidation reactions, as well as being a common air pollutant.^{2,3,18–21} Our results show that Nb doped TiO₂ with fairly high doping concentrations (10–20 mol %) is a poor solar active photocatalyst material compared to TiO₂, despite the fact that Nb doping extends the optical absorption into the visible and utilizes a larger portion of the sunlight. Furthermore, we discuss in detail the importance of cation coordination and bonding of intermediate reaction products for the total photocatalytic oxidation rate using an interplay between FTIR measurements and density functional theory (DFT) calculations. Even though our results are negative in the sense that the quantum yield for acetone degradation is lowered upon Nb doping, we believe that our results are instructive and point to intrinsic difficulties that must be solved when the cation doping route is used to improve the photocatalytic performance of TiO₂.

2. Experimental Section

2.1. Material Synthesis. Alkoxides and ammonia were used as purchased (Aldrich), while the 99.5% ethanol was dried by distillation over CaH₂. The alkoxide precursors were weighed and mixed in an Ar-filled glovebox (Braun MB 200). Ti(OPrⁱ)₄ was mixed with Nb(OEt)₅ to the desired proportions under inert atmosphere, and ethanol was added to provide 1 M solutions. After heating at 60 °C for 1 h, the solutions were cooled to ambient temperature, and concentrated ammonia providing 5 H₂O per alkoxo group was added under vigorous stirring. The material was subsequently heated at 80 °C for 8 h and ultrasonically dispersed before it was put in an autoclave for hydrothermal treatment at 200 °C for 15 h. After cooling, the autoclaved material was again ultrasonically treated and concentrated under vacuum, and carbowax was added to yield a white paste. Before use, the paste was diluted with water to a dry content of ca. 0.7 wt %. The solution of the nondoped titania was also made acidic by the addition of a small amount of acetic acid.

Diluted pastes of 0, 10, 15, and 20 mol % NbO_{2.5} in TiO₂ were deposited as thin films on either Si(100) wafers (10 × 10 × 0.25 mm³) or α-Al₂O₃ substrates (25 × 1 mm²) by evaporating the 0.7 wt % sol in air and subsequently heat-treated in air at 450 °C for 30 min.

2.2. Materials Characterization. The structural, optical, and chemical properties of the synthesized materials were characterized by a range of different techniques. Scanning electron microscope (SEM) images were obtained with a FEG-SEM Leo 1550 Gemini instrument. Transmission electron microscopy (TEM) was done with a JEOL 2000 FXII instrument equipped with an EDS module (Link AN 1000). Reflectance micro-Raman spectra of samples heat-treated in air for 30 min at 723 K were recorded with a Renishaw 2000 spectrometer using a 783 nm laser diode light source. Grazing incidence X-ray diffractograms (GI-XRD) were obtained for samples heat-treated at 723 K with a Siemens D-5000 instrument. After phase identification of the materials, the XRD peak positions and (*hkl*) values were used as input to extract the lattice parameters with the software Fullprof.²² Room-temperature UV–vis spectra were measured in transmission mode with a Perkin-Elmer Lambda 19 instrument on thin films deposited on α-Al₂O₃ windows. The deposition of films was made in the same way as those deposited on the silicon wafers for FTIR analysis. The absorbance in the

film, *A* (where *A* = −log(*T*)), was measured using a noncoated α-Al₂O₃ window as a transmission reference, viz., $A_{\text{film}} = -\log(10^{-A_{\text{Al2O3+film}} + A_{\text{Al2O3}}}) = A_{\text{Al2O3+film}} - A_{\text{Al2O3}}$. Finally, X-ray photoelectron spectroscopy (XPS) measurements were made with a Kratos Axis Ultra electron spectrometer using a mono Al K_α source operated at 225 W and a low-energy electron gun for charge compensation. High-resolution scans were acquired using a pass energy of 20 eV and an energy resolution of 0.1 eV. The hybrid lens mode was used for all measurements. The binding energy scale was calibrated against the C 1s line of aliphatic carbon, set at 285.0 eV. Atomic concentrations (atom %) were derived from photoelectron peak areas using Shirley or linear background subtraction, the instrumental sensitivity factors, and a transmission function appropriate to the acquisition conditions.

2.3. Reactivity Measurements. Fourier transform infrared (FTIR) transmission measurements were made in a vacuum-pumped spectrometer (Bruker IFS 66v/S) equipped with a transmission reaction cell, which allowed for simultaneous UV and IR illumination of the sample. The IR light was collected with an LN₂ cooled narrow-band HgCdTe detector. Repeated FTIR spectra were measured with 4 cm^{−1} resolution and 135 scans (corresponding to 30 s measurement time per spectra) and 30 s dwell time between consecutive spectra. All spectra were smoothed with a Savitzky–Golay algorithm using a 9-point window. Deconvolution of FTIR peaks was performed by fitting the experimental curves with Gauss–Lorentzian curves, after appropriate baseline corrections of the spectra.

The FTIR spectra reported here were all acquired with the samples kept at 299 K in a 100 mL/min feed flow of synthetic air (20% O₂ and 80% N₂) through the reaction cell. The feed flow was controlled by a set of mass flow controllers, and the gas purity was 99.994% (N₂) and 99.999% (O₂). The gas was used as delivered without further purification. Prior to each measurement, the samples were cleaned at 673 K for 15 min in synthetic air and subsequently cooled to 299 K in the same feed. The TiO₂ samples are thus pre-oxidized.

Acetone (analytical grade, Scharlau) was added to the feed gas through a home-built gas generator, consisting of a capillary tube in contact with a liquid acetone reservoir maintained at constant temperature (*T* = 303 ± 0.2 K) controlled by a PID regulator. The independently calibrated acetone injection in the feed obtained with these parameters was 0.29 ± 0.02 mg/min, which corresponds to an ideal steady-state concentration of 1232 ± 109 ppm in the feed. No other gas species than acetone were detected mass-spectrometrically with this gas evaporation setup. In each experiment, the sample was exposed to 15 min of acetone. After acetone dosing, the sample was left for 20 min in the pure feed gas before the solar light illumination was started. In all measurements, the FTIR background was collected on a clean sample during 1 min (265 scans) in a synthetic air feed at 299 K.

2.4. Solar Light Illumination. Simulated solar light was generated by a Xe arc lamp source operated at 200 W and a set of filters (AM1.5). To reduce the infrared part of the emission spectrum, the light was first directed through a 75-mm-long water filter. The light was collected into a fused silica fiber bundle and directed onto the sample cell through a CaF₂ window at an angle of 25° to the surface normal. The measured photon power after the fiber bundle was 173.5 mW/cm² between λ = 200 and 800 nm as measured with a calibrated thermopile detector. Taking into account the absorption efficiency of the detector (96%) and the UV transmission through the cell window (92%), we determined the photon power on the sample to be

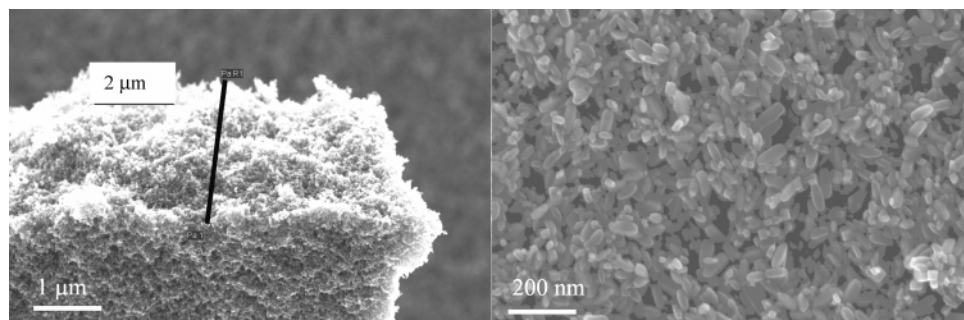


Figure 1. SEM images of the nanostructured anatase TiO₂ film doped with 10%NbO_{2.5}: Cross-sectional view showing the films thickness (left), and top-view showing the elongated particle structure (right).

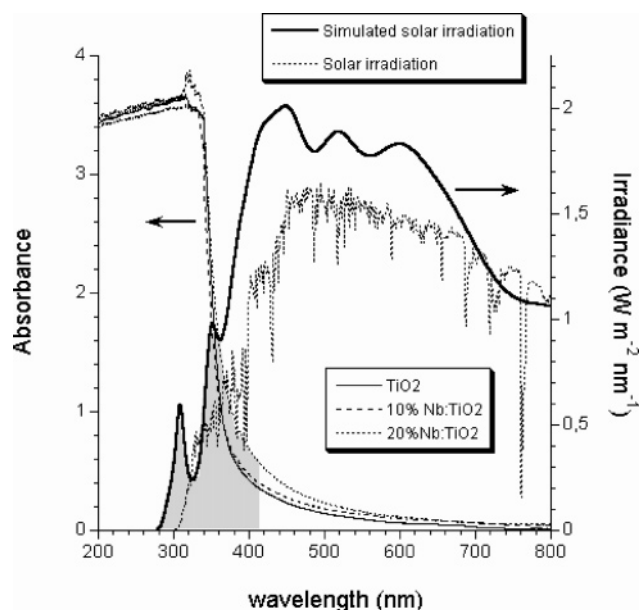


Figure 2. Left ordinate: The measured absorbance, $A(\lambda)$, of the Nb:TiO₂ films used in the present study. Right ordinate: Measured power spectrum (irradiance), $P(\lambda)$, of the simulated solar light (AM1.5) used in the present study (solid line) compared to the corresponding solar irradiance spectrum (dashed line).²³ The effective energy available for photocatalysis (i.e., the absorbed photon flux above the optical band gap) is indicated by the gray area.

166 mW/cm². The measured irradiance spectrum through the filter combination and fiber optics is given in Figure 2 (right ordinate), together with the corresponding AM1.5 standard solar irradiance spectrum.²³

2.5. DFT Calculations. To gain further insight into the electronic and structural properties of the key surface species, we have performed density functional theory (DFT) calculation under periodic boundary conditions (using the program package CASTEP from Accelrys, Inc.). Exchange and correlation effects have been included within the generalized gradient approximation (GGA) developed by Perdew and Wang.²⁴ The atoms are represented by ultrasoft nonlocal pseudopotentials in the Kleinman–Bylander fully separable form.²⁵ The electronic wave functions were expanded in terms of plane-waves, and the electronic minimization was performed using a band-by-band conjugate-gradients minimization technique.²⁶ The specific \mathbf{k} -points were generated by the Monkhorst–Pack scheme, which produces a uniform mesh of \mathbf{k} -points in the reciprocal space.²⁷ The adsorbate and the upper two atomic layers of the surface were allowed to fully relax in all of the calculations using the BFGS algorithm (Broyden–Fletcher–Goldfarb–Shanno).²⁸ The rest of the atoms were kept fixed in order to hold the characteristics of the crystal lattice. Moreover, the covalent bond

TABLE 1: Unit Cell Dimension Determined from GI-XRD and Particle Size of TiO₂–NbO_{2.5}

	a (Å)	b (Å)	c (Å)	particle size (nm)
TiO ₂	3.785	3.785	9.497	18 ^a /15–30 ^b
10 mol % Nb	3.802	3.802	9.523	23 ^a /15–70 ^b
20 mol % Nb	3.816	3.816	9.529	35 ^a

^a The particle size is estimated from broadening of the (101) peak in anatase using the Scherrer equation, introducing a Scherrer factor of 0.9 and obtaining the internal error from the line-width of the Si reference. ^b Particle size as determined from TEM measurements. Here, some of the Nb-doped particles appear elongated, and the dimensions indicate the spread in the long-axis dimension (see Figure 1).

strengths within the bonds between the adsorbate and the surface, as well as within the adsorbate as a function of adsorption, were estimated by calculating the electron bond populations by projecting the plane-wave states onto the localized basis set by means of Mulliken electron population analysis.²⁹

3. Results and Discussions

3.1. Material Characterization. In Figure 1 is shown SEM images of the 10% Nb doped films. Analysis of the SEM images showed that the pure films were ca. 2.5 μm thick consisting of ca. 20 nm spherical-like particles with crystallite edges clearly resolvable for pure TiO₂.

The Nb doped TiO₂ films consist of slightly larger, elongated (“rectangular”) structures. From the weight and the volume derived from the deposited area and film thickness, an estimated porosity of ca. 47% was obtained. A rough estimation of the surface area (assuming spherical particles) gives a theoretical surface area of ca. 62 m² g^{−1}. The estimated geometrical surface area decreases somewhat with increased Nb content, which is in qualitative agreement with the change of the particle shapes. TEM measurements give particle sizes of 15–30 nm for pure anatase TiO₂ and 15–70 nm for 10% NbO_{2.5}:TiO₂. Mostly spherical TiO₂ particles are found in TEM, while 10% and 20% Nb doped TiO₂ contain both elongated and spherical particles. The average particle sizes are compiled in Table 1.

The thickness determined from SEM is in good agreement with independent measurements of the measured interference pattern due to reflections at the film interface in transmission FTIR, which yields $d = 2.1, 1.6$, and $1.9 \mu\text{m}$ for TiO₂, 10% Nb:TiO₂, and 20% Nb:TiO₂, respectively, as obtained from the equation

$$d = \frac{N}{2n(\bar{\nu}_1 - \bar{\nu}_2)} \quad (1)$$

where N = number of interference maximum (or minima)

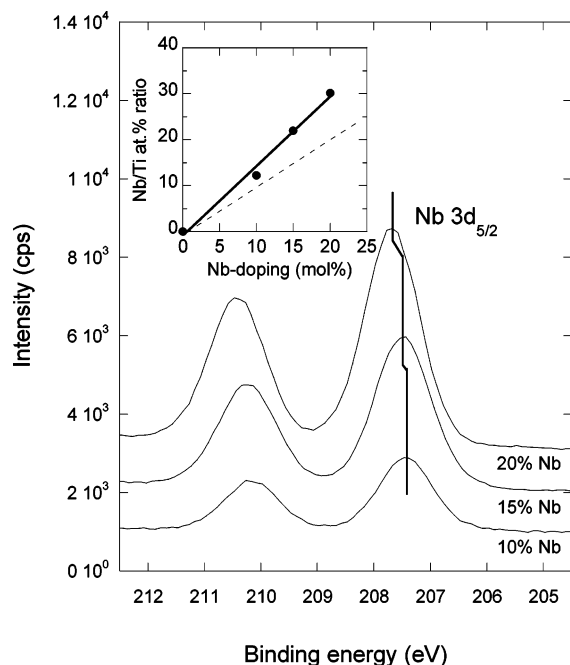


Figure 3. Nb 3d_{5/2} XPS spectra for Nb doped TiO₂ thin films. The inset shows the measured (solid line) and ideal Nb/Ti concentration ratio as a function of NbO_{2.5} doping concentration (see text).

between the wavenumbers $\bar{\nu}_1$ and $\bar{\nu}_2$ (in units of cm⁻¹), and n = refractive index of film ($n = 2.5$ for anatase).

The measured absorbance, A , of the films from the UV–vis measurements is plotted in Figure 2 (left ordinate). For indirect-gap semiconductors, such as TiO₂, $\alpha h\nu = (h\nu - E_g)^2$, where α is the absorption coefficient.³⁰ A least-squares fit of $\sqrt{\alpha h\nu} \propto h\nu$ yielded a straight line near the absorption threshold, which confirmed that the Nb doped materials are also indirect-gap semiconductors. By extrapolation of the least-squares fit lines, the optical absorption edges were determined to be $E_g = 3.15$ eV (394 nm), 3.11 eV (399 nm), and 3.02 eV (411 nm) for TiO₂, 10% Nb:TiO₂, and 20% Nb:TiO₂, respectively. The data for the Nb doped films varies from batch to batch, but the red-shift due to Nb doping occurs consistently. The red-shift in the UV–vis spectrum and the resulting pale yellow color of the Nb doped films are typical for pentavalent Nb oxide (in contrast to the transparent films reported in ref 17) and suggest that a Burstein–Moss effect due to conduction band filling does not occur (or is minor) in our sol–gel synthesis route with NbO_{2.5} doping.^{31,32} Since charge injection from HOMO Nb derived states (notably 5s) may be expected to occur for single-atom Nb doping, this further supports that NbO_{2.5} nuclei are dissolved in the TiO₂ lattice and that Nb=O clusters are responsible for the red-shift of the optical absorption. This provides an explanation of the different results compared with those reported by Furubayashi et al.¹⁷

In Figure 3 is shown XPS Nb 3d spectra for the 10, 15, and 20 mol % Nb doped TiO₂ films. The binding energy values, BE, for Nb 3d_{5/2} for Nb metal and Nb oxides are BE(Nb(0)) = 202.2 ± 0.3 eV, BE(Nb(II)O) = 203.7 ± 0.8 eV, BE(Nb(IV)-O₂) = 206.1 ± 0.9 eV, and BE(Nb(V)₂O₅) = 207.4 ± 0.4 eV.³³ The observed BE increases from 207.4 to 207.7 eV as a function of doping. It is evident that only peaks associated with pentavalent Nb and tetravalent Ti appear in XPS for all samples. The inset shows Nb/Ti atom % ratio as a function of Nb doping. It is seen in Figure 3 that the Nb concentration increases as a function of Nb doping slightly more than what is expected for homogeneous doping, which suggests a slight surface enrichment of Nb at least at the highest doping concentrations.

From the combined GI-XRD and Fullprof calculations, the cell dimensions for the undoped TiO₂ were determined to $a = b = 3.785$ Å and $c = 9.497$ Å, which correspond well to the cell reported in the literature for TiO₂ synthesized with a sol–gel technique.³⁴ GI-XRD measurements of the films heat-treated to 450 °C for 30 min showed that all compositions yielded films purely of the anatase modification, which was also corroborated by Raman spectroscopy, which revealed only peaks associated with anatase ($\nu_{\text{obs}} = 638$ cm⁻¹ (E_g), 515 cm⁻¹ (A_{1g}), 395 cm⁻¹ (B_{1g}), 195 cm⁻¹ (E_g), and 142 cm⁻¹ (E_g)). Nb doping caused only slight modifications of the peaks in the A_{1g} and E_g mode regions. A substantial increase of the calculated a , b , and c parameters was obtained by increasing Nb content, which together with the XPS results indicates that the Nb doping results in pentavalent Nb oxide incorporated in the anatase TiO₂ lattice (Table 1). This is in agreement with recent results for Nb doped anatase films.¹⁷ However, the expansion of the unit cell is not as large as for the laser-deposited thin films in ref 17, which further supports our XPS results that some Nb accumulates in the surface region in our sol–gel synthesized films. We have shown previously that very high levels of substitution of NbO_{2.5} in anatase TiO₂ can be achieved with the basic, rapid hydrolysis route with subsequent heating in air, instead of autoclaving.³⁵ In this case, up to 35–40 mol % NbO_{2.5} could be doped in anatase TiO₂, while, at higher levels, a distorted rutile-like phase was obtained. The cell dimensions increased with increasing Nb content in that series also, but were ca. 0.01 Å larger in all directions, compared to the present data. Also, the cell edges obtained for TiO₂ prepared by other techniques seem to vary to some degree, which has been ascribed to different kinds of vacancies.³⁴ Since the ionic radius of Nb⁵⁺ is similar to Ti⁴⁺, it is expected that Nb acts as a donor atom when dissolved in TiO₂ because of charge transfer from the Nb 5s derived state to the conduction band. Thus, the most probable model would involve a substitutional doping with Nb⁵⁺ in Ti⁴⁺ positions and the formation of cation vacancies (V) to maintain charge neutrality, corresponding to the overall stoichiometry Ti_{1-x}(Nb_{0.8x} + V_{0.2x})O₂. Interstitial doping is less likely to occur, since it should be difficult to fit them into the structure while maintaining the anatase structure. A distortion of the lattice should take place; in particular, at the high doping concentration the structure should collapse.

The absorbed photon power was determined from the measured irradiance of the lamp source and the UV–vis spectra. Below E_g , it has been shown³⁶ that the scattering coefficient is small in comparison to the absorption coefficient for small anatase TiO₂ nanoparticles. If it is assumed that this holds in the present case, an upper limit of the total absorbed photon flux, F_{ph} , above E_g for each of the films can be estimated from

$$F_{\text{ph}} = \int dF_{\text{ph}}(\lambda) d\lambda = \int A(\lambda) \times P(\lambda) d\lambda \quad (2)$$

where $P(\lambda)$ is the measured irradiance from the solar light source, and the integration is done from $\lambda_{\text{min}} = 200$ nm (below the irradiance threshold for the simulated solar light) and $\lambda_{\text{max}} = \lambda_g$ (corresponding to the measured optical band gap, E_g , for each of the material). The total absorbed photon flux obtained is schematically depicted by the gray area in Figure 2 and is calculated to be 6.5, 7.1, and 9.2 mW/cm², respectively, for TiO₂, 10% Nb:TiO₂, and 20% Nb:TiO₂, respectively (1.2·10¹⁶, 1.3·10¹⁶, and 1.7·10¹⁶ photons s⁻¹ cm⁻²). Thus, an upper limit of the enhanced absorbed photon flux due to Nb doping for light with energies above the band gap, $h\nu > E_g$, is estimated to be 9% and 43% for 10% and 20% Nb doping, respectively.

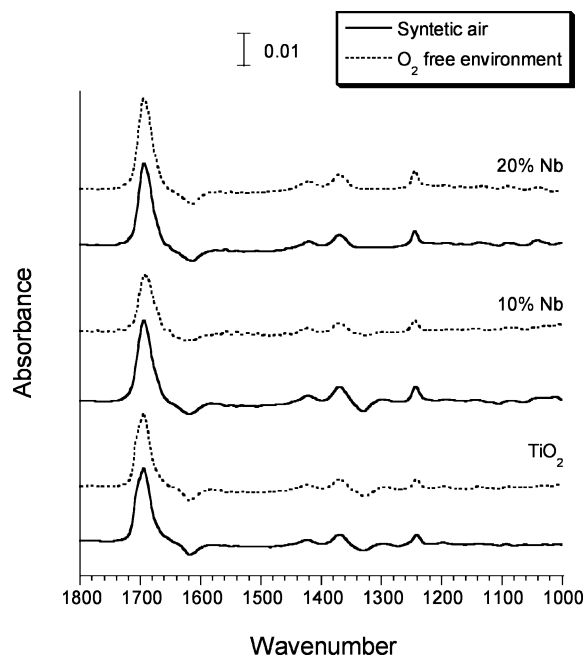


Figure 4. FTIR spectra obtained on anatase TiO_2 and two $\text{Nb}:\text{TiO}_2$ films after 15 min acetone adsorption and 15 min stabilization in a synthetic air feed. Peak assignments are given in Table 2.

For comparison, the corresponding solar AM1.5 irradiance spectrum is also shown in Figure 2.

3.2. Acetone Adsorption. Figure 4 shows FTIR spectra recorded after 15 min of acetone dosing on the three different $\text{Nb}:\text{TiO}_2$ films (0, 10, and 20 mol % Nb, respectively) at a surface temperature of 299 K in synthetic air and subsequent equilibration in synthetic air.

In the course of equilibration in synthetic air, some acetone molecules desorb, and the spectra in Figure 4 corresponds to 0.84, 0.81, and 0.82 ML acetone for 0%, 10%, and 20% Nb doped TiO_2 , respectively (see below). This is in agreement with recent temperature programmed desorption (TPD) results, where it was reported that acetone started to desorb from rutile $\text{TiO}_2(110)$ at $T > 300$ K.³⁷ From the FTIR spectra, we conclude that acetone adsorbs associatively on TiO_2 , since all major infrared absorption peaks for condensed acetone are present with no additional vibrational losses.³⁸ In contrast, on 20% $\text{NbO}_{2.5}:\text{TiO}_2$, weak bands at 1042 and 1091 cm^{-1} appear, which indicate small amounts of dissociation of the methyl groups and formation of methoxy species on these surfaces.^{39,40} We note that there is no difference—within our experimental uncertainties—of dosing acetone with O_2 present or not on pure anatase TiO_2 , i.e., our data cannot validate a small O_2 -induced dissociation pathway, as suggested for a reduced rutile $\text{TiO}_2(110)$ exposed to O_2 in vacuo.³⁷ This may be due to the limited accuracy inherent in atmospheric studies on nanoparticle TiO_2 films or an intrinsic difference between the rutile and anatase polymorphs and/or the reactivity of O_2 bonded at reduced sites.³⁷ The observed acetone frequencies and band assignments for the samples are presented in Table 2.

In Figure 5, the growth of the carbonyl $\nu(\text{C}=\text{O})$ absorption band as a function of dosing time is shown. Clear differences can be seen between the spectra for the different materials. For the Nb doped film, a new carbonyl $\nu(\text{C}=\text{O})$ peak appears, which is shifted toward lower wavenumbers in comparison to the pure TiO_2 . Deconvolution of the FTIR peaks reveals three peaks associated with the $\nu(\text{C}=\text{O})$ absorption band (dashed curves in Figure 4) at 1707, ~ 1695 , and 1672 cm^{-1} , where the latter peak is exclusively observed on the Nb doped samples and remains

TABLE 2: IR Frequencies and Band Assignments for Acetone Adsorption on $\text{Nb}:\text{TiO}_2$ after 15 min Exposure at 299 K Followed by Stabilization in Synthetic Air for 20 min^a

band assignment	TiO_2 (cm^{-1})	10% $\text{Nb}:\text{TiO}_2$ (cm^{-1})	20% $\text{Nb}:\text{TiO}_2$ (cm^{-1})
$\nu(\text{C}-\text{C})$	1243	1243	1245
$\delta_s(\text{CH}_3)$	1369	1370	1369
$\delta_a(\text{CH}_3)$	1423	1422	1422
$\nu(\text{C}=\text{O})$	1694	1696	1696
Ti: η^1 -coordination	—	1672	1672
Nb: η^1 -coordination	1707	—	—
multilayer			
$\nu_s(\text{CH}_3)$	2925	2923	2923
$\nu_a(\text{CH}_3)$	2976	2976	2977

^a The coverages correspond to $\theta_{\text{Ac}} = 0.84$ on TiO_2 , $\theta_{\text{Ac}} = 0.81$ on 10% $\text{Nb}:\text{TiO}_2$, and $\theta_{\text{Ac}} = 0.82$ on 20% $\text{Nb}:\text{TiO}_2$.

at the same frequency during the complete dosing time and for all Nb doping concentrations. The peak at 1707 cm^{-1} observed on TiO_2 after 15 min dosing is close to the corresponding $\nu(\text{C}=\text{O})$ in liquid acetone and signals multilayer adsorption.⁴¹ The absorption peak at ~ 1695 cm^{-1} shifts to higher wavenumbers with increasing coverage indicative of repulsive adsorbate—adsorbate interactions.

The sensitivity of the $\nu(\text{C}=\text{O})$ frequency to acetone coverage, Nb doping, and the similarity of the main absorption bands with condensed acetone suggests that the acetone molecule bonds to the surface to coordinatively unsaturated cation sites (c.u.s.) through the O atom on the carbonyl group in the well-known η^1 -coordination.^{19,21,42,43} The appearance of the red-shifted $\nu(\text{C}=\text{O})$ peak on the Nb doped samples indicates higher coupling energy (stronger bonding) of the carbonyl group with the surface and a concomitant weakened intramolecular bond. To further validate our interpretation of the $\nu(\text{C}=\text{O})$ mode, we have also measured CO adsorption on doped and undoped TiO_2 . However, at room temperature, the resulting CO coverage was too small to detect the CO mode. This is in agreement with our DFT calculation of CO bonded to c.u.s. Nb atoms on 9 mol % $\text{Nb}:\text{TiO}_2(001)$, where it is found that the Nb—CO adsorption energy is small ($E_a = -59$ kJ/mol) and even nonfavorable in the case of Ti—CO ($E_a > 0$). Furthermore, the calculated shift of the CO frequency from 2102 cm^{-1} (corresponding to gas phase) to 1824 cm^{-1} supports our assignment of the different $\nu(\text{C}=\text{O})$ modes for acetone and demonstrates a charge redistribution from the C=O bond to the O—Nb bond (electron population of 0.01).

Figure 6 shows the uptake curves of acetone as a function of time on the three different films. Here, the contributions of the $\nu(\text{C}=\text{O})$ absorption band originating from different chemical environments were used to probe the amount of adsorbed η^1 -acetone adsorption at different surface sites.

We use the abbreviations Ac—Ti [η^1 -coordination to Ti], Ac—Nb [η^1 -coordination to Nb], and Ac—Ac [multilayer adsorption] to distinguish the different types of molecules. The amount of each species was derived from the peak areas obtained by deconvoluting the $\nu(\text{C}=\text{O})$ bands in Figure 5, where the positions of the Ac—Nb and Ac—Ac peaks were fixed, but all other parameters (fwhm, peak shape, and Ac—Ti position) were allowed to vary freely. We assume that the 1695 cm^{-1} peak on TiO_2 approaches an asymptotic coverage, θ_{Ac} , as a function of dosing time that corresponds to 1 ML ($\theta_{\text{Ac}} = 1$), which is defined to be 1 acetone molecule per fivefold coordinated surface Ti site in the (101) plane, where the number of Ti sites, N_s , is $N_s \approx 7 \cdot 10^{14}$ molecules cm^{-2} .^{37,44} By analogy, the asymptotic value of the sum of the 1695 and 1672 cm^{-1} peaks is defined to be $\theta_{\text{Ac}} = 1$ on the Nb doped films. Upon

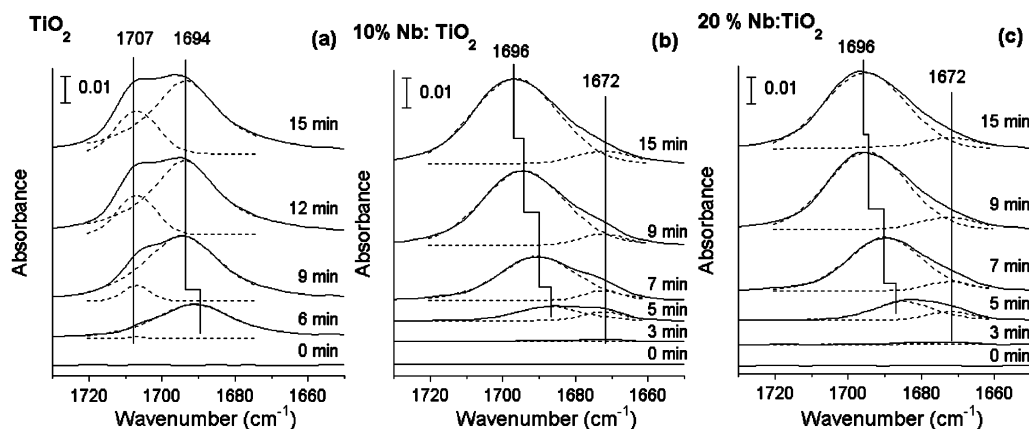


Figure 5. FTIR spectra showing the growth of the $\nu(\text{C}=\text{O})$ acetone peak as a function of acetone dosing time on (a) TiO_2 , (b) 10% Nb:TiO₂, and (c) 20% Nb:TiO₂. A new $\nu(\text{C}=\text{O})$ peak evolves at 1672 cm^{-1} on Nb doped TiO₂. A multilayer peak at 1707 cm^{-1} appears on TiO₂ after extended exposures.

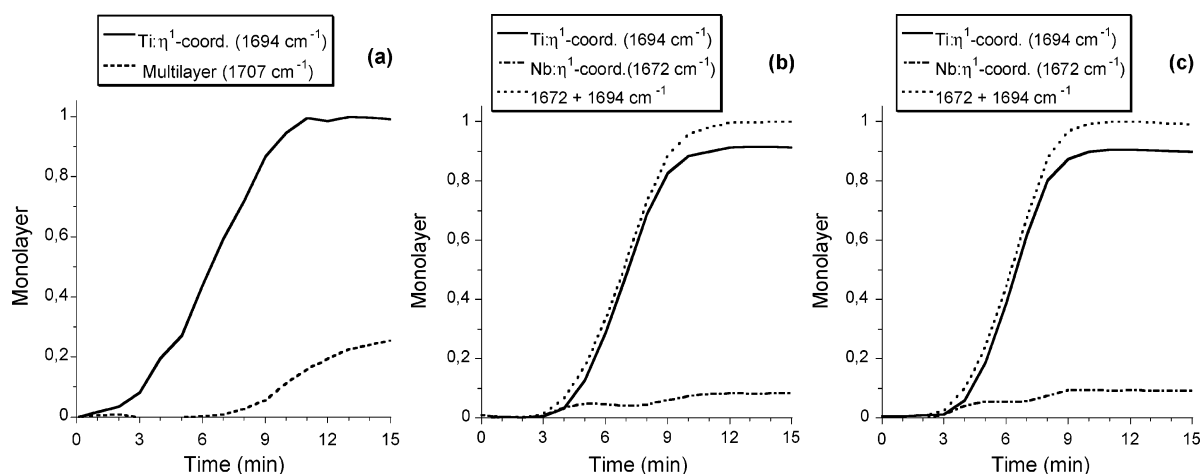


Figure 6. Acetone adsorption uptake curves on (a) TiO_2 , (b) 10% Nb:TiO₂, and (c) 20% Nb:TiO₂ as a function of time, as deduced from the $\nu(\text{C}=\text{O})$ absorption bands.

stabilization in pure N_2 or synthetic air, the multilayer peak almost disappears on TiO_2 , and $\theta_{\text{Ac}} = 0.84$ remains on the surface (cf. Figure 4). It is evident from Figure 6 that the amount of Ac–Nb species builds up simultaneously to the Ac–Ti species. This suggests that acetone is mobile at room temperature and populates the energetically more favorable Ac–Nb sites first. The integrated Ac–Nb peak intensity at 1672 cm^{-1} is not proportional to the Nb concentration and is only about 10% higher on the 20% Nb:TiO₂ film compared to the 10% Nb:TiO₂ film; at 20% Nb doping, a coverage of $\theta_{\text{Ac}} \approx 0.1$ Ac–Nb molecules are inferred from Figure 6. With the XPS results taken into account, which show an increase by a factor of 2.5 of the Nb/Ti concentration going from 10% to 20% Nb doped TiO₂, this shows that surface enrichment of Nb with increasing Nb doping does not lead to exposure of proportionally more c.u.s. Nb atoms. A possible explanation of this is that acetone dissociates proportionally more on the 20% Nb doped TiO₂ sample, which is also seen in the FTIR spectra in Figure 4. The estimated NbO_x stoichiometry plotted in Figure 3 indicates formation of substoichiometric NbO_x ($x < 2.5$) at the surface with increasing doping concentration, which could expose (more) reactive Nb sites and account for the enhanced dissociation.

With increasing coverage, a multilayer of acetone starts to build up on TiO_2 , but not on the Nb doped samples despite an equivalent exposure. Since the particle size increases with Nb doping, an increased total surface area of the porous films cannot explain the apparent different saturation coverages; nor can it

be explained by a higher desorption rate on the Nb doped films, since acetone bonding to c.u.s. Nb sites is stronger than on corresponding Ti sites. We therefore attributed this difference to thermal acetone dissociation on the Nb doped samples, as evidenced by the weak absorption bands due to $\nu_{\text{a}}(\text{CO})$ and $\nu_{\text{s}}(\text{CO})$ in adsorbed methoxy groups (dissociated from acetone) at 1042 and 1091 cm^{-1} in Figure 3 and a weak shoulder at 2960 cm^{-1} .^{18,39}

3.3. Solar Light Decomposition of Acetone. Figure 7 shows FTIR spectra obtained after different times of solar light illumination for the three different Nb:TiO₂ samples after acetone adsorption (corresponding to Figure 3). It is immediately apparent that the rate of decomposition is much higher on the pure TiO_2 film than the Nb doped films, as indicated by the disappearance of the acetone $\nu(\text{C}=\text{O})$ and $\nu(\text{C}-\text{C})$ peaks at 1694 and 1223 cm^{-1} , respectively. Simultaneously, new absorption bands due to intermediate oxidation products appear upon solar light illumination. After 60 min of illumination, all traces of acetone and surface-bonded intermediates have vanished in the FTIR spectra on TiO_2 , while significant amounts of acetone and intermediates are still present on the Nb doped films.

To elucidate the difference in the photocatalytic activity of the different materials, the formation and disappearance of acetone and the intermediate surface adducts as deduced from FTIR spectra were analyzed in detail. The FTIR peak areas for pure TiO_2 have been grouped according to their shape and time dependence in Figure 8. The time evolution of the various peaks

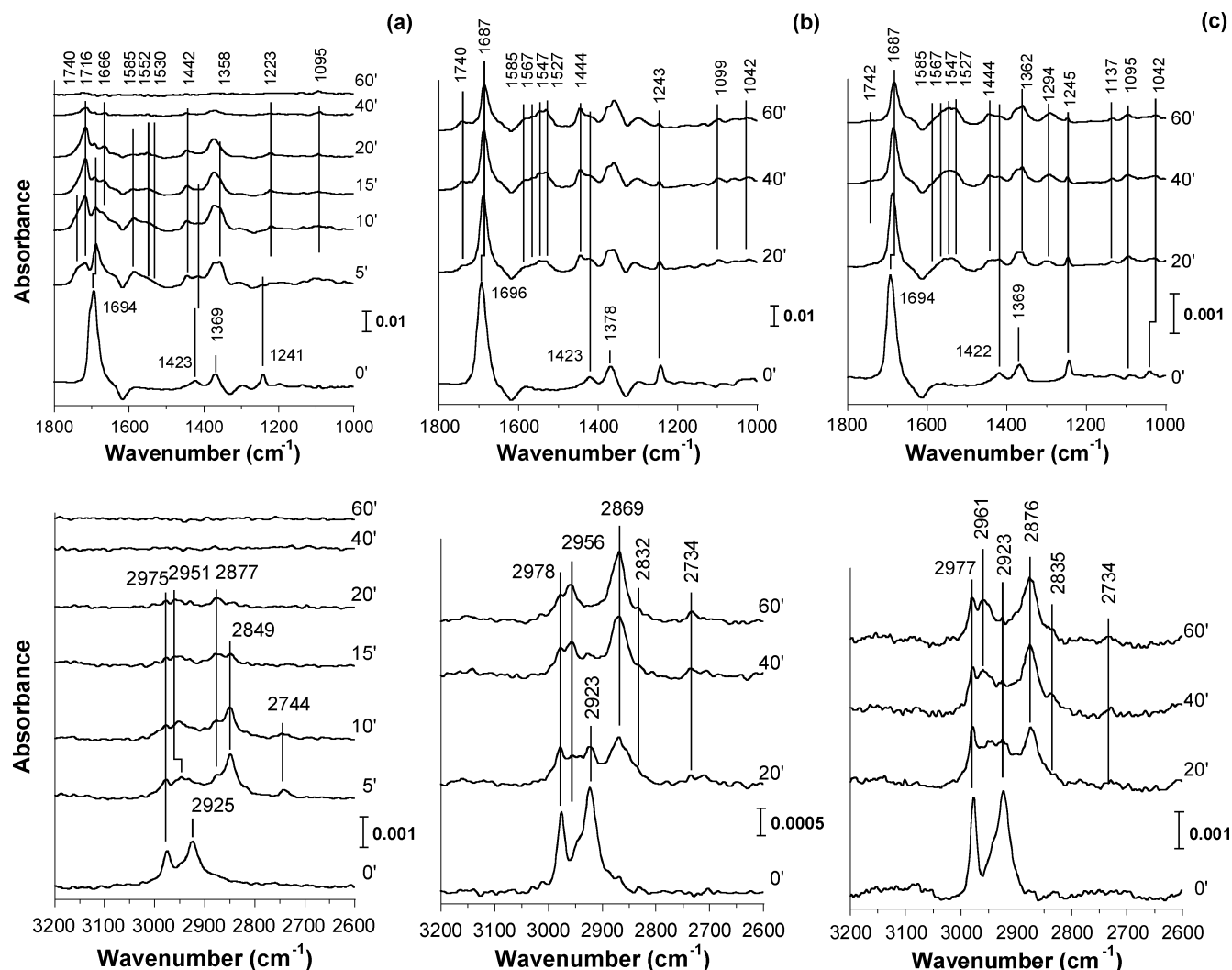


Figure 7. FTIR spectra obtained at different times after the start of solar light illumination ($t = 0$) for (a) left panel, pure TiO_2 ; (b) middle panel, 10% Nb:TiO₂; and (c) right panel, 20% Nb:TiO₂. The bottom curves for $t = 0$ min in the 1000–1800 cm^{-1} region are the same curves as in Figure 3. The initial coverages were $\theta_{\text{Ac}} = 0.88$, 0.81, and 0.82, respectively.

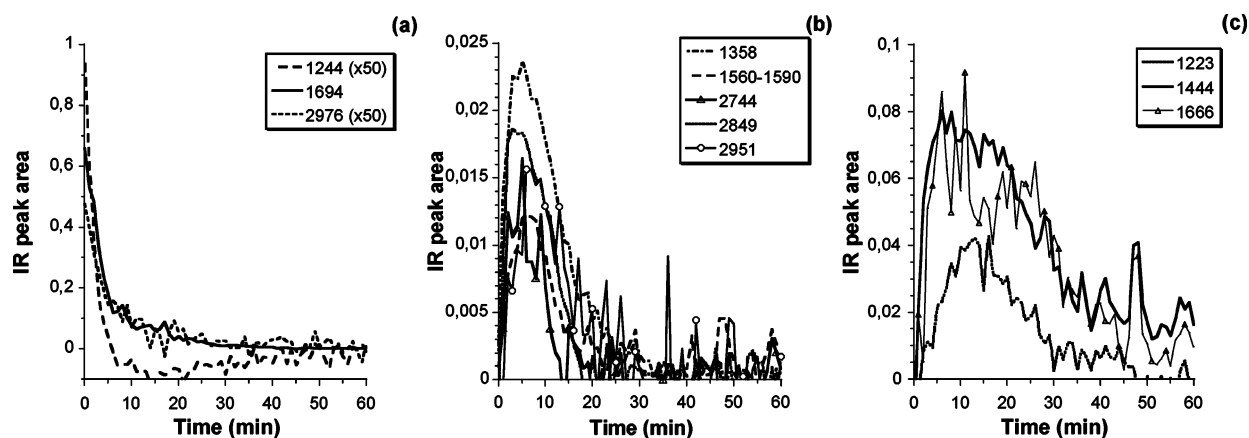


Figure 8. Time evolution of the integrated FTIR peak areas shown in Figure 7 as a function of illumination time of the TiO_2 film. The peaks are grouped into different categories depending on their kinetic behavior: (a) peaks associated with acetone, (b) peaks due to aldehydes and coordinated formate, and (c) peaks associated with coordinated carbonate and bicarbonate species. The wavelength-dependent penetration depth (d_λ) has been corrected for by applying a linear dependence of the penetration depth and wavelength ($d_\lambda \propto \lambda$).

can be grouped into four main categories on TiO_2 depending on their appearance and disappearance as a function of illumination time.

(1) In the first class, acetone and its associated infrared bands decrease rapidly with illumination time (Figure 8a).

(2) In the second class, peaks that have an intensity maximum

at ca. 6 min appear (Figure 8b). This coincides with the time where all acetone has been decomposed on TiO_2 . Among them, we find peaks that can be related to coordinated formate and aldehyde species.⁴⁵ In particular, in the 1540–1590 cm^{-1} region, the $\nu_{\text{a}}(\text{COO})$ bands due to bridged bidentate and monodentate formate and bicarbonate species are expected to appear.^{45–47}

TABLE 3: IR Band Assignments of Intermediates Formed on the TiO₂ Films after Solar Light Illumination

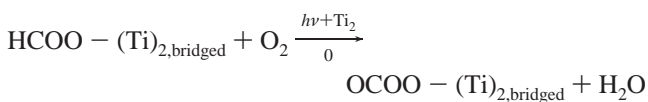
molecule	band assignment	wavenumber [cm ⁻¹]	$\Delta = \nu_a(\text{COO}) - \nu_s(\text{COO})$	proposed structure
			[cm ⁻¹]	
bicarbonate	$\nu_a(\text{CO})$	1528	180	bridged
	$\nu_s(\text{CO})$	1444		
	$\nu(\text{OH})$	3635		
carbonate	$\nu(\text{CO})$	1666	446	bridged
	$\nu(\text{CO}) + \delta(\text{OCO})$	1223		
formate	$\nu_a(\text{CO})$	1552, 1585	194, 227	bridged, ion
	$\nu_s(\text{CO})$	1358		
	$\nu(\text{CH})$	2877		
	$\nu_a(\text{CO}) + \delta(\text{CH})$	2951		
aldehyde	$\nu(\text{CHO})$	2744	-	monodentate
	$\nu(\text{CO})$	2735		

Detailed analysis reveals absorption bands at 1585 and 1552 cm⁻¹, which are due to the $\nu_a(\text{COO})$ in HCOO⁻ ion and bidentate bridged HCOO (μ -formate), respectively. The associated formate $\nu_a(\text{COO}) + \delta(\text{CH})$ combination band appears at 2951 cm⁻¹ and the $\nu(\text{CH})$ band at 2877 cm⁻¹.^{45–48} The absorption band at 2744 cm⁻¹ is attributed to the typical $\nu(\text{CHO})$ stretching frequency in an aldehyde.^{48,49} The 1740 cm⁻¹ absorption band apparent in Figure 7 falls into the same category 2 group as the 2744 cm⁻¹ and is also attributed to formaldehyde (not shown).

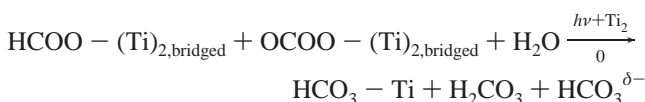
(3) The third class of species (Figure 8c) reaches a maximum concentration after 12 min illumination and is mainly due to bicarbonate and coordinated carbonate species.^{45–47} The peak at 1442 cm⁻¹ can be assigned to the symmetric carbonate mode in bicarbonate ions in hydrogen-bonded networks ([HCO₃^{-δ}...H—O]).⁴⁵ Furthermore, the 1666, 1223, and 1095 cm⁻¹ bands are assigned to the $\nu(\text{CO})$ modes in bidentate bridged carbonate (μ -carbonate) on the basis of previous reports (see below).^{46,48,50}

(4) Finally, we note that the most persistent peak on TiO₂ is the one at 1715 cm⁻¹, which reaches a maximum after 17 min. The origin of this peak is not settled, but it is tempting to associate these bands to asymmetric coordinated CO₂ species.^{45,47,51}

The band assignment on TiO₂ is summarized in Table 3. On the basis of the results in Table 3 and Figure 8, it is evident that on TiO₂ the rate of decomposition of formate, bicarbonate, and carbonate species varies considerably. Evidently, formate is transformed into carbonate



In the course of the reaction, water is produced, and the R—CO₂ species reacts with OH and H₂O to form a mixed layer of bicarbonate and carbonate species



Pursuing the same analysis as in Figure 8 for Nb doped films reveals that both the rates of formation and of decomposition of formate, carbonate, and bicarbonate species are significantly slower on the Nb doped films. In Figure 9 are shown the concentrations of μ -formate (1552 cm⁻¹), μ -carbonate (1666 and 1223 cm⁻¹ peaks), and H-bonded bicarbonate (1444 cm⁻¹)

on Nb doped TiO₂ as a function of decomposed acetone molecules relative to the corresponding concentration on TiO₂. Values > 1 (< 1) indicate a higher (lower) surface concentration compared to pure TiO₂ and can be interpreted as stabilization (destabilization) of the surface species due to Nb. Here, each absorption band has been corrected for variations in the IR absorption in each measurements by normalizing the peaks to the integrated $\nu(\text{C}=\text{C})$ peaks in acetone at $t = 0$ (prior to illumination). The most striking difference here is that on the Nb:TiO₂ films μ -carbonate is destabilized, while the H-bonded bicarbonate concentration is higher at a given amount of decomposed acetone. Furthermore, μ -formate (1552 cm⁻¹) appears stabilized by Nb doping, but the uncertainty is greater here because of overlapping absorption bands. The large increase of the relative μ -formate concentration in Figure 9 with increasing acetone conversion is due to the depletion of formate on TiO₂ and the simultaneous accumulation on Nb doped TiO₂. Finally, the weaker 1585 cm⁻¹ peak on Nb doped TiO₂ suggests that HCOO⁻ ions are readily transformed to bicarbonate or μ -formate.

To further corroborate our spectral band assignment and understand the observed trends, we have calculated the adsorption energies (E_a) and the electron population for μ -formate and μ -carbonate bonded to c.u.s. Ti only and with one bond to a Nb surface atoms (see Figure 10).

The μ -coordination bonding geometry of formate to rutile TiO₂(110) is well-known.^{46,52,53} We assume that this is also the preferred coordination on the anatase phase, and we use the non-reconstructed (001) facet to mimic the bonding to crystalline anatase nanoparticles. We employ the same bonding geometry in the Nb doped sample. The results from our DFT calculations are shown in Table 4. It is seen that E_a for μ -formate is similar for TiO₂ and Nb doped TiO₂, while the metal—O bonding strength as measured by the electron population is strengthened by ca. 10% upon Nb doping, in fair agreement with the experimental results. In contrast, carbonate formation is significantly favored on the Nb doped films compared to pure TiO₂ (by ca. 145 kJ/mol). Our FTIR results indicate, however, that μ -carbonate is significantly more stable on TiO₂. This can be understood by inspecting the electron population, which shows that the metal—O bond is substantially weaker on Nb doped TiO₂ than on pure TiO₂ (by more than 20%). The result is that bicarbonate rather than carbonate formation is favored on Nb doped TiO₂, which is in good agreement with the FTIR data.

3.4. Rate of Acetone Decomposition and Quantum Yield.

In Figure 11a are shown plots of $\ln(A/A_0)$ vs time, t , for the different materials, where A_0 denoted the deconvoluted peak area of the acetone $\nu(\text{C}=\text{O})$ absorption band ($\propto \theta_{\text{Ac}}$).

For the Nb doped films, the curves are linear during the whole illumination period, while it is linear only during the first 7 min for pure TiO₂. This suggests that the initial decomposition rate can be described by a first-order reaction, viz.

$$-\frac{d\theta_{\text{Ac}}}{dt} = k_{\text{dec}}\theta_{\text{Ac}} \quad (3)$$

where k_{dec} is the rate constant for decomposition of acetone on the films and is determined from a linear least-squares fit to the data in Figure 11a. The quantum yield, ϕ , is defined as the ratio of the rate of (initial) photoreaction to the rate of absorbed photons at a given wavelength.⁵⁴ We define here the solar light (AM1.5) quantum yield, $\phi_{\text{AM1.5}}$, obtained by illuminating our thin films precovered with acetone (coverage, θ_i) and illuminated by simulated solar light (AM1.5) as

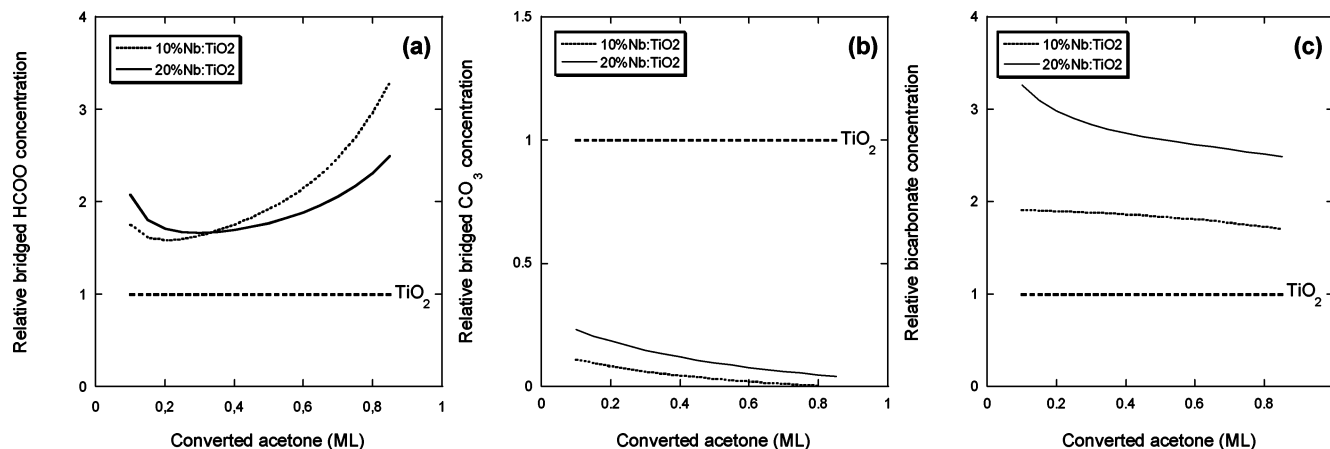


Figure 9. Concentration of μ -formate, μ -carbonate, and H-bonded bicarbonate, respectively, on 10% and 20% Nb doped TiO_2 films divided by the corresponding concentration on the pure TiO_2 film as a function of decomposed acetone molecules. The difference in IR transmission for different samples has been corrected for by normalizing each spectrum to the initial acetone coverage.

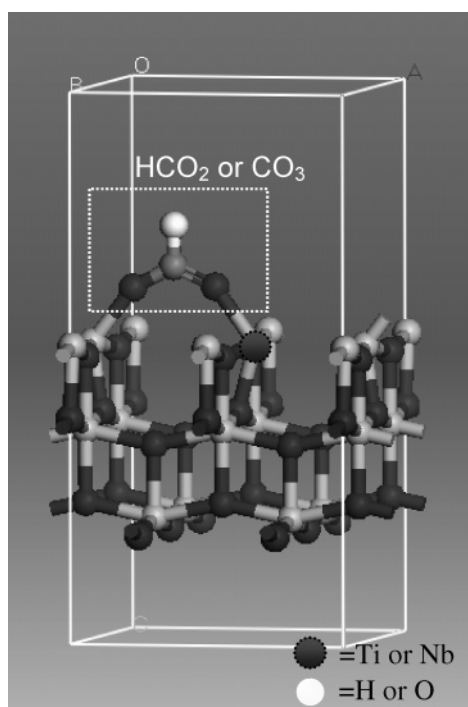


Figure 10. Formate and carbonate adsorption geometry used in the DFT calculations of bidentate bridge-bonded species on anatase TiO_2 -(001). One of the O atoms in the μ -coordinated species is either coordinated to a Ti or a Nb surface atom.

$$\phi_{\text{AM1.5}} = \frac{K_{\text{dec}}}{F_{\text{ph}}} \quad (4)$$

where K_{dec} is the rate of acetone decomposition per unit area of illuminated film, and F_{ph} is the rate of photon absorption per unit area (section 3.1). However, since F_{ph} neglects scattering (albeit small above E_g , as discussed above), ϕ is actually a lower-limit quantum yield, which is sometimes referred to an apparent quantum yield.⁵⁴ $K_{\text{dec},i}$ ($i = \text{TiO}_2$, 10% Nb:TiO₂, or 20% Nb:TiO₂) can be estimated from the equation

$$K_{\text{dec},i} = kK_{\text{dec},i}\theta_{\text{Ac},i}N_sA_{s,i} \quad (5)$$

where $A_{s,i}$ is the total surface area of illuminated material within the UVA penetration depth, d_λ (ca. 1 μm)⁵⁵

$$A_{s,i} = N_s\pi d_i^2 \quad (6)$$

TABLE 4: Calculated Adsorption Energies and Bond Electron Population for Bidentate Bridge Bonded Formate and Carbonate on Anatase TiO_2 (001) and 9 at % Nb:TiO₂

	HCOO (μ -formate)	CO ₃ (μ -carbonate)
	Anatase TiO_2 (001)	
adsorption energy	−579 kJ/mol	−724 kJ/mol
electron population		
C–O _{i,ii}	0.87, 0.88	0.78, 0.76
C–O _{iii}		1.09
Ti _{ii} ···O _i	0.30	0.42
Ti _{ii} ···O _{ii}	0.32	0.42
TiO ₂ (bulk)	0.70	0.70
	9% Nb Anatase TiO_2 (001)	
adsorption energy	−579 kJ/mol	−868 kJ/mol
electron population		
C–O _{i,ii}	0.86, 0.80	0.82, 0.76
C–O _{iii}		1.10
Ti _{ii} ···O _i	0.35	0.39
Nb _i ···O _{ii}	0.32	0.28
NbO ₂ (bulk)	0.73	0.73

where N_i is the total number of particles within the illuminated volume, and d_i is the average (spherical) particle diameter (Table 1). The acetone decomposition rates and estimated quantum yields are reported in Table 5.

It is evident that the quantum yield for acetone decomposition is 1 order of magnitude higher on pure TiO_2 than the Nb doped TiO_2 samples. This contrasts the results presented above where it was shown that the Nb doped films absorb a larger fraction of the solar light and that the carbonyl bonding to c.u.s. Nb sites are stronger than to Ti sites. Both of these observations may be anticipated to promote acetone decomposition. That this is not the case indicates most likely that the $e-h$ recombination rate is increased, which in turn may be related to an increased defect density and/or creation of local NbO_x induced states in the band gap. Other explanations include delocalized states in the band gap below the O_2 affinity level, but recent reports of the formation of a visible transparent Nb induced degenerate semiconductor¹⁷ suggest that our Nb doped materials (with dissolved $\text{NbO}_{2.5}$) in this case must have very different band structures. Of the above explanations, we attribute the inferior activity to the Nb=O cluster formation and the concomitant cation vacancy formation, which act as recombination centers. We propose a model where Ti–O–Nb=O··· cation vacancy ···O=Nb–O–Ti structures form starting with niobyl groups at the surface with the O atoms pointing inward toward a metal vacancy. The cause of the band gap shift and yellowish color

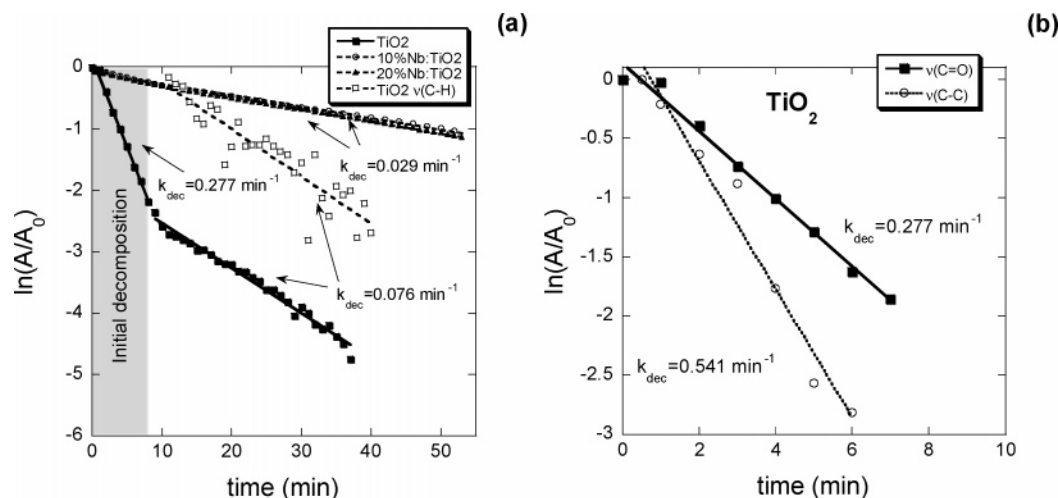


Figure 11. Plots of the normalized logarithmic decay of the acetone $\nu(\text{C}=\text{O})$ absorption band as a function of time (a) and a comparison of the decay of the $\nu(\text{C}=\text{O})$ and $\nu(\text{C}-\text{C})$ modes (b). For TiO_2 , all acetone is decomposed within 7 min of solar light illumination ("initial decomposition"). The slower rate at $t > 7$ min is due to oxidation of intermediates.

TABLE 5: The Initial First-Order Decomposition Rate Constant ($t < 7$ min) and the Solar Light Quantum Yield for the Pure and Nb Doped TiO_2 Films

film material	decomposition rate, k_{dec} [min^{-1}]	decomposition rate, K_{dec} [molecules $\text{s}^{-1} \text{ cm}^{-2}$]	quantum yield, $\phi_{\text{AM1.5}}$ [molecules photons $^{-1}$]
TiO_2	0.277	6.4×10^{14}	0.053
10% Nb:TiO ₂	0.029	5.1×10^{13}	0.004
20% Nb:TiO ₂	0.029	3.4×10^{13}	0.002

are thus due to these $\text{O}-\text{Nb}=\text{O}$ centers. A cause for the slight surface enrichment seen in XPS at 10–20% doping concentrations may be due to the formation of line defects when no more $\text{Nb}=\text{O}$ chains can be accommodated in the structure. Instead, $\text{Nb}=\text{O}$ clusters align parallel to the surface along these line defects. On the basis of this model, an inferior activity with even small amounts of Nb may be anticipated. In this model, we do not rule out that formation of heterojunctions of NbO_x and TiO_2 occurs at the surface at the highest doping concentrations and may thus contribute to the observed electron transport properties.

The interpretation of the quantum yield is complicated by the slight Nb surface enrichment, which is expected to result in part of the acetone adsorbed on a Nb oxide-like surface; it cannot be excluded that this fraction is responsible for the ca. 10% dark acetone dissociation inferred from section 3.2. Interestingly, the slope of the curve (k_{dec}) for TiO_2 in Figure 11a changes abruptly above ca. 7 min and attains a new value, which is also well-described by a linear curve. By comparing the decay of the $\nu(\text{C}=\text{O})$ and integrated $\nu(\text{C}-\text{H})$ absorption bands for $t = 10$ –40 min (where the $\nu(\text{C}-\text{H})$ peaks were integrated between 3000 and 2700 cm^{-1}), it is seen that they decay with the same rate, which now is almost a factor of 4 lower compared to $t < 7$ min. This shows that at $t = 10$ –40 min decomposition of intermediates such as μ -formate completely dictates the infrared spectra, and the contribution from the $\nu(\text{C}=\text{O})$ band is minor in the 1700–1600 cm^{-1} region. At $t > 40$ min, the $\nu(\text{C}-\text{H})$ peaks are small, which is expected, since the amount of $\text{C}-\text{H}$ species is decreased and mainly (bi)carbonates remain on the surface (section 3.2). In contrast, on the Nb doped films, no discernible decrease of k_{dec} is observed during the whole illumination period (60 min), where the rate-determining step for total acetone oxidation is the initial acetone decomposition step. This is also evident from Figure 9, where it is seen that the concentration of the final surface species carbonate and bicarbonate on the Nb doped films decreases relative to TiO_2 as the initial photodegradation of acetone proceeds.

Finally, we show in Figure 11b a comparison of the decomposition rate determined from the $\nu(\text{C}=\text{O})$ and $\nu(\text{C}-\text{C})$ peak areas between $t = 0$ and $t = 7$ min. From Figure 11b, it is seen that the rate of disappearance of the methyl groups also follows a first-order reaction, but the rate of disappearance is twice as fast as that for the carbonyl mode. This shows that the two methyl groups dissociate simultaneously as the carbonyl group reacts and form μ -coordinated surface compounds. This observation further supports previous reports that acetone decomposition does not occur by direct H abstraction.³⁷

Conclusions

Doping of anatase TiO_2 with $\text{NbO}_{2.5}$ by the sol–gel route results in a distorted anatase structure and a unit cell expansion with pentavalent Nb oxide incorporated in the lattice with a slight surface enrichment of Nb at the highest doping concentration (20 mol % $\text{NbO}_{2.5}$). The Nb doped films absorb up to 40% more of the visible light than the anatase films and appear slightly yellowish, which is attributed to $\text{O}-\text{Nb}=\text{O}$ centers. Acetone binds more strongly to Nb sites than to Ti sites with a carbonyl η^1 -coordination, which results in a small amount of acetone dissociation on the Nb doped films. Despite the larger UV–vis absorption and the stronger surface interaction, the estimated quantum yield is an order of magnitude smaller on the Nb doped films. The lower photocatalytic activity is attributed to an increased $e-h$ recombination rate due to the $\text{Nb}=\text{O}$ cluster and vacancy site formation in the anatase lattice. In the course of the photodegradation reaction, a variety of surface products form. The photodegradation reaction starts with methyl group dissociation and subsequent formation of bidentate bridge-bonded formate and carbonate bonded. Reaction with OH and H_2O yields bicarbonate which appears as H-bonded species. The relative concentration of these surface species are different on pure and Nb doped TiO_2 and can be explained by their different heats of formation and bonding strength to the surface metal atom. In general, it appears that it is very difficult

to improve the photocatalytic activity of TiO₂ by cation doping, since charge transfer to the conduction band (ref 17), defect and vacancy site formation (because of Nb=O clusters), and bond formation at the surface (e.g., an increased formate bond strength) all must be tuned appropriately. This has hitherto not proven possible with Nb doping, employing different doping methods.

Acknowledgment. This work was supported by the Swedish Department of Defence (project no. 430-A4515).

References and Notes

- (1) Fujishima, A.; Hashimoto, K.; Watanabe, T. *TiO₂ Photocatalysis. Fundamentals and Applications*; BKC, Inc.: Tokyo, 1999.
- (2) Teichner, S. J.; Formenti, M. In *Photoelectrochemistry, Photocatalysis, and Photoreactors*; Schiavello, M., Ed.; Reidel Publishing Company: Dordrecht, 1985; p 457 ff.
- (3) *Photocatalytic Purification and Treatment of Water and Air*; Ollis, D. F., Al-Ekabi, H., Eds.; Elsevier: Amsterdam, 1993.
- (4) Anpo, M. In *Green Chemistry*; Tundo, P., Anastas, P., Eds.; Oxford University Press: Oxford, 2000.
- (5) Anpo, M. *Bull. Chem. Soc. Jpn.* **2004**, *77*, 1427.
- (6) Asahi, R.; Morikawa, T.; Ohwaki, T.; Aoki, K.; Taga, Y. *Science* **2001**, *293*, 269.
- (7) Lindgren, T.; Mwabora, J. M.; Avendano, E.; Jonsson, J.; Hoel, A.; Granqvist, C.-G.; Lindqvist, S.-E. *J. Phys. Chem. B* **2003**, *107*, 5709.
- (8) Sakthivel, S.; Kisch, H. *Angew. Chem., Int. Ed.* **2003**, *42*, 4908.
- (9) Khan, S. H. M.; Al-Shahry, M.; Ingler, W. B., Jr. *Science* **2002**, *297*, 2243.
- (10) Hattori, A.; Yamamoto, M.; Tada, H.; Ito, S. *Chem. Lett.* **1998**, *27*, 707.
- (11) Subbarao, S. N.; Yun, Y. H.; Kershaw, R.; Dwight, K.; Wold, A. *Inorg. Chem.* **1979**, *18*, 488.
- (12) Umebayashi, T.; Yamaki, T.; Itoh, H.; Asai, K. *Appl. Phys. Lett.* **2002**, *81*, 454.
- (13) Anpo, M.; Nakaya, H.; Kodama, S.; Kubokawa, Y.; Domen, K.; Onishi, T. *J. Phys. Chem.* **1986**, *90*, 1633.
- (14) Miyauchi, M.; Takashio, M.; Tobimatsu, H. **2004**, *20*, 232.
- (15) Venkataraj, S.; Drese, R.; Liesch, C.; Kappertz, O.; Jayavel, R.; Wuttig, M. *J. Appl. Phys.* **2002**, *91*, 4863.
- (16) Granqvist, C. G. *Handbook of Inorganic Electrochromic Systems*, 2nd ed.; Elsevier: Amsterdam, 2002.
- (17) Furubayashi, Y.; Hitosugi, T.; Yamamoto, Y.; Inaba, K.; Kinoda, G.; Hirose, Y.; Shimada, T.; Hasegawa, T. *Appl. Phys. Lett.* **2005**, *86*, 252101.
- (18) Busca, G. *Catal. Today* **1996**, *27*, 457.
- (19) Coronado, J. M.; Kataoka, S.; Tejedo-Tejedor, I.; Anderson, M. A. *J. Catal.* **2003**, *219*, 219.
- (20) El-Maazawi, M.; Finken, A. N.; Nair, A. B.; Grassian, V. H. *J. Catal.* **2000**, *191*, 138.
- (21) Zaki, M. I.; Hasan, M. A.; Pasupulety, L. *Langmuir* **2001**, *17*, 768.
- (22) Rodriguez-Carvajal, J. *Physica B* **1993**, *192*, 55.
- (23) <http://redc.nrel.gov/solar/spectra/am1.5/>.
- (24) Perdew, J. P.; Wang, Y. *Phys. Rev. B* **1992**, *42*, 13244.
- (25) Kleinman, L.; Bylander, D. M. *Phys. Rev. Lett.* **1982**, *48*, 1425.
- (26) Teter, M. P.; Payne, M. C.; Allan, D. C. *Phys. Rev. B* **1989**, *40*, 12255.
- (27) Monkhorst, H. J.; Pack, J. D. *Phys. Rev. B* **1976**, *13*, 5188.
- (28) *Molecular Modeling and Simulation: An Interdisciplinary Guide*; Antman, S. S., Marsden, J. E., Sirovich, L., Eds.; Springer-Verlag: New York, 2002.
- (29) Segall, M. D.; Shah, R.; Pickard, C. J.; Payne, M. C. *Phys. Rev. B* **1996**, *54*, 16317.
- (30) Tang, H.; Prasad, K.; Sanjinès, R.; Schmid, Lévy, F. *J. Appl. Phys.* **1994**, *75*, 2042.
- (31) Burstein, E. *Phys. Rev.* **1954**, *93*, 632.
- (32) Moss, T. S. *Proc. Phys. Soc. London, Ser. B* **1954**, *67*, 775.
- (33) Wagner, C. D.; Naumkin, A. V.; Kraut-Vass, A.; Allison, J. W.; Powell, C.; Ramble, J. R., Jr., Eds. *NIST Standard Reference Database 20*, version 3.4 (Web version); National Institute of Standards and Technology: Gaithersburg, MD, 20899; accessed August 2003.
- (34) Milella, F.; Gallardo-Amores, J. M.; Baldi, M.; Busca, G. *J. Mater. Chem.* **1998**, *8*, 2525.
- (35) Leideborg, M.; Westin, G. Preparation of Ti-Nb-O Nano Powders and Studies of the Structural Development on Heat Treatment. *Ceramics: Getting into the 2000's, Part B; Advances in Science and Technology*, Vol. 14; *Proceedings of the 9th CIMTEC World Ceramics Congress and Forum on New Materials*; Vincenzini, P., Ed.; June 14–19, 1998, Florence, Italy.
- (36) Loddo, V.; Addamo, M.; Augugliaro, V.; Di Paola, A.; García-López, E.; Marci, G.; Palmisano, L.; Schiavello, M. Heterogeneous Photocatalysis: Optical Characterisation of polycrystalline Photocatalysts for Pollutant Degradation in Aqueous Media. 8th International Conference on Solar Energy and Applied Photochemistry, 2005, Luxor, Egypt.
- (37) Henderson, M. A. *J. Phys. Chem. B* **2004**, *108*, 18932.
- (38) Stein, S. E. Infrared Spectra. NIST Mass Spec Data Center; National Institute of Standards and Technology: Gaithersburg, MD; June 2005.
- (39) Rusu, C.; Yates, J. T., Jr. *J. Phys. Chem. B* **2000**, *104*, 12292.
- (40) Glisenti, J. *J. Mol. Catal., A* **2000**, *153*, 169.
- (41) Stein, S. E. Infrared Spectra. NIST Mass Spec Data Center; *NIST Chemistry WebBook, NIST Standard Reference Database Number 69*; Linstrom, P. J., Mallard, W. G., Eds.; National Institute of Standards and Technology: Gaithersburg, MD, March 2003; <http://webbook.nist.gov>.
- (42) Henderson, M. A. *Surf. Sci.* **1998**, *400*, 203.
- (43) Griffith, D. M.; Rochester, C. *J. Chem. Soc., Faraday Trans. 1* **1978**, *74*, 403.
- (44) Diebold, U. *Surf. Sci. Rep.* **2003**, *48*, 53.
- (45) Österlund, L. *Int. J. Nanotechnol.* In press.
- (46) Busca, G.; Lorenzelli, V. *Mater. Chem.* **1982**, *7*, 89.
- (47) Nakamoto, K. *Infrared and Raman Spectra of Inorganic and Coordination Compounds*, 5th ed.; John Wiley & Sons: New York, 1997.
- (48) Tanaka, K.; White, J. M. *J. Phys. Chem.* **1982**, *86*, 4708.
- (49) Sokrates, G. *Infrared Characteristic Group Frequencies*, 2nd ed.; John Wiley & Sons: Chichester, 1994.
- (50) Davydov, A. A. *Infrared Spectroscopy of Adsorbed Species on the Surface of Transition Metal Oxides*; John Wiley & Sons: New York, 1990.
- (51) Mascetti, J.; Tranquille, M. *J. Phys. Chem.* **1988**, *92*, 2177.
- (52) Hayden, B. E.; King, A.; Newton, M. A. *J. Phys. Chem. B* **1999**, *103*, 203.
- (53) Rotzinger, F. P.; Kesselman-Truttmann, J. M.; Hug, S. J.; Shklover, V.; Gratzel, M. *J. Phys. Chem. B* **2004**, *108*, 5004.
- (54) Serpone, N.; Emeline, A. V. *Int. J. Photoenergy* **2002**, *91–131*.
- (55) Courbon, H.; Formenti, M.; Juillet, F.; Lisachenko, A. A.; Martin, J.; Teichner, S. *J. Kinet. Catal.* **1973**, *14*, 84.